Ground states of Heisenberg spin clusters from projected Hartree-Fock theory

Shadan Ghassemi Tabrizi[1,*] and Carlos A. Jiménez-Hoyos[2,†]

[1]*Technische Universität Berlin, Institut für Chemie, Theoretische Chemie – Quantenchemie, Sekr. C7, Strasse des 17. Juni 135, 10623 Berlin, Germany*

[2]*Department of Chemistry, Wesleyan University, Middletown, Connecticut 06459, USA*

(Received 17 September 2021; revised 6 January 2022; accepted 10 January 2022; published 27 January 2022)

We apply the projected Hartree-Fock theory (PHF) for approximating ground states of Heisenberg spin clusters. Spin-rotational, point-group, and complex-conjugation symmetry are variationally restored from a broken-symmetry mean-field reference, where the latter corresponds to a product of local spin states. A fermionic formulation of the Heisenberg model furnishes a conceptual connection to PHF applications in quantum chemistry and detailed equations for a self-consistent field optimization of the reference state are provided. Different PHF variants are benchmarked for ground-state energies and spin-pair correlation functions of antiferromagnetic spin rings and three different polyhedra, with various values of the local spin-quantum number s. Although PHF is not suitable to study the thermodynamic limit (where it reduces to the conventional HF results), the low computational cost and the compact wave-function representation make PHF a promising complement to existing approaches for ground states of finite spin clusters, particularly for large local spin s and a moderately large number of sites N. The present work may also motivate future explorations of more accurate post-PHF methods for Heisenberg spin clusters.

DOI: 10.1103/PhysRevB.105.035147

I. INTRODUCTION

The theoretical modeling of exchange-coupled spin clusters, as realized in a growing number of magnetic molecules, is based on spin Hamiltonians [1]. Isotropic coupling of Heisenberg type, $\hat{H} = \sum_{i<j} J_{ij}\hat{\mathbf{s}}_i \cdot \hat{\mathbf{s}}_j$, is usually the dominant term. Numerically exact calculations of spectroscopic or thermodynamic properties are limited to small systems, due to the quick growth of the Hilbert space with the number of spin centers. When exact diagonalization (ED) is not feasible, the choice of a suitable approximation technique is determined by the system specifics (size, coupling topology, etc.) and by the magnetic properties of interest [2]. For ground states of one-dimensional (1D) systems, density matrix renormalization group (DMRG) [3] is the most important variational method. For 2D systems (see, e.g., the family of Keplerate molecules with icosidodecahedral magnetic cores [4–6] V_{30}, Cr_{30}, or Fe_{30}), convergence is much slower [7,8], and depends on the formal ordering of sites. Dynamical DMRG (DDMRG) [9,10] can be used to predict transition probabilities. As an example, DDMRG was used for the modeling of inelastic neutron scattering (INS) on an Fe_{18} spin ring [11]. Very accurate thermal averages for relatively large systems are accessible by the finite-temperature Lanczos method (FTLM) [12–14], but some of the largest magnetic molecules are out of reach of this method. In contrast to FTLM, quantum Monte Carlo methods [15] are basically limited to systems lacking frustration [16]. The Fe_{30} molecule represents a suitable example to list a few additional methods. ED is impossible, because Fe_{30} hosts thirty $s = \frac{5}{2}$ centers, leading to a Hilbert-space dimension of $\mathcal{N} = 6^{30} \approx 2 \times 10^{23}$. To a first approximation, the rotational-band model (RBM) [17], which uses a simplified Hamiltonian, correctly describes the low-temperature magnetization staircase [18]. Some features of the INS spectra are captured by molecular spin-wave theory [19,20]. Even a classical treatment explains certain experimental data of Fe_{30} [21]. Compared to one specific correlated product-state approach [22], DMRG yields lower ground-state energies in the different S_z sectors, if a sufficient number of density-matrix eigenstates is kept [8]. However, convergence with respect to this number could not be reached [8].

The perspective on approximation methods is further broadened by regarding a fermionic formulation of the Heisenberg model, which motivates the adoption or modification of static-correlation methods from electronic-structure theory or other fields of many-body physics. The most intuitive fermionization for $s = \frac{1}{2}$ converts the spin Hamiltonian into the covalent-space Pauling-Wheland valence-bond model [23] ("canonical VB", see Theory section). The VB formulation mimics the original far more complex *ab initio* electronic-structure problem from which the effective Heisenberg model emerges. Configuration-interaction (CI) [24,25], variational Monte Carlo (VMC) [26,27], resonating valence-bond theory (RVB) [28], or variants of coupled-cluster theory (CC) [29] invoke the VB formulation, and thereby formally extend the Hilbert space of the spin model. In mean-field (Hartree-Fock, HF) solutions for extended systems, the physical constraint of one fermion occupying each site is generally fulfilled on average only [30]. The VMC method optimizes a mean-field wave function in the presence of an operator that projects out unphysical (ionic) contributions [31]. Other methods for finite systems involve only covalent states, which

*ghastab@mailbox.tu-berlin.de
†cjimenezhoyo@wesleyan.edu

have exactly one fermion per site. For example, CI, RVB or CC work exclusively on covalent configurations; in this sense, fermionization is not essential, but conceptually helpful from a quantum chemist's perspective.

Here, we approximate ground states of Heisenberg spin clusters by projected Hartree-Fock theory (PHF) [32]. PHF restores all or a subset of symmetries from a mean-field reference in a variation-after-projection (VAP) fashion. We are mostly concerned with the optimization of a general unentangled spin-product state in the presence of a combined spin and point-group projection operator. This allows us to target the ground state in each symmetry sector, where the latter is defined by spin and point-group quantum numbers. We can also explicitly restore the antiunitary complex-conjugation symmetry, which is not associated with any quantum-number or a projection-operator in the usual sense. By formulating the Heisenberg model in the spirit of canonical VB, we establish an intuitively useful connection to PHF applications in quantum chemistry. PHF is a black-box method with a compact representation of the wave function and comes at a mean-field computational cost (with a prefactor that depends on the number of points in the symmetry-projection grid). In our present diagonalization strategy for optimization, the formation of the effective Fock matrix, see the Supplemental Material (SM) [33], scales linearly with the number of spin sites (the scaling becomes quadratic when working with a projector for cyclic symmetry in spin rings). In conjunction with the promising benchmark results presented below, these appealing features could make PHF a useful complementary method for studying ground states and, to some extent, low-temperature properties of certain types of spin clusters. We however emphasize that the method is not capable of describing properties in the thermodynamic limit, such as spin-gapped phases.

The following Theory section briefly recapitulates PHF theory and provides a few computational details. The Results and Discussion section describes applications of different variants of PHF to the antiferromagnetic Heisenberg model (AFH) for spin rings and three different polyhedra. Rather than aiming for new insights into any specific system, the emphasis is on providing benchmark results. We offer a detailed self-consistent field (SCF) diagonalization-based optimization algorithm in the SM.

II. THEORY

PHF theory. The simple idea behind PHF originated in quantum chemistry [34,35]: find a broken-symmetry mean-field state $|\Phi\rangle$ which is energetically optimal for the application of a symmetry-projection operator $\hat{P}$. Invoking the concept of self-consistent symmetry [36–38], the optimal PHF reference $|\Phi\rangle$ will generally break all those symmetries[1] that one chooses to restore [32]. Recent *ab initio* studies [39–43] were based on a formalism that expresses the energy of the projected state as a function of the single-particle density matrix [32]. The PHF equations [32] assume a general second-quantized Hamiltonian with single-particle (quadratic) and two-particle (quartic) terms, see Eq. (1). VB formulations of the Heisenberg model comply with this form (see next section).

$$\hat{H} = \sum_{lm} t_{lm}\hat{c}_l^\dagger \hat{c}_m + \frac{1}{2}\sum_{klmn} \hat{c}_k^\dagger \hat{c}_l^\dagger \hat{c}_m \hat{c}_n [kn|lm]. \tag{1}$$

In quantum-chemical terminology, a Slater determinant $|\Phi\rangle$ that completely breaks spin symmetry is of generalized HF (GHF) type. PHF variants that restore spin (S), complex-conjugation (K), or point-group (PG) symmetry, or combinations of these, from a GHF-type reference, are called SGHF, KSGHF, PGKSGHF [32,44], etc. The lowest variational energy is afforded by PGKSGHF, because it works with the largest symmetry group. We leave the somewhat more complicated issue of K-symmetry restoration aside in this section, but see Ref. [43] and Sec. 2 of the SM for details. Note that KGHF is equivalent to the complex molecular-orbital method (CMO) of Hendeković [45,46].

The energy E, Eq. (2), of the projected state, $|\Psi\rangle = \hat{P}|\Phi\rangle$, must be minimized with respect to $|\Phi\rangle$.

$$E = \frac{\langle\Phi|\hat{H}\hat{P}|\Phi\rangle}{\langle\Phi|\hat{P}|\Phi\rangle}. \tag{2}$$

For PG projection, we are only concerned with 1D irreducible representations Γ. The respective projector is $\hat{P}_\Gamma$, Eq. (3), where h is the order of the group, $\chi_\Gamma(g)$ is the character of group element g, and $\hat{G}(g)$ is the corresponding operation [47]:

$$\hat{P}_\Gamma = \frac{1}{h}\sum_{g=1}^{h} \chi_\Gamma^*(g)\hat{G}(g). \tag{3}$$

Multidimensional irreducible representations become relevant for spin projection onto $S > 0$ sectors. The projector $\hat{P}_M^S$ for spin S and magnetic quantum number M is expanded in terms of transfer operators,

$$\left|\Psi_M^S\right\rangle = \hat{P}_M^S|\Phi\rangle = \sum_K f_K \hat{P}_{MK}^S|\Phi\rangle, \tag{4}$$

which are conveniently parameterized by Euler angles, Eq. (5) [48],

$$\hat{P}_{MK}^S = \frac{2S+1}{8\pi^2}\iiint d\alpha d\beta d\gamma \sin(\beta) \times D_{MK}^{S*}(\alpha,\beta,\gamma)e^{-i\alpha\hat{S}_z}e^{-i\beta\hat{S}_y}e^{-i\gamma\hat{S}_z}. \tag{5}$$

Optimization of $|\Phi\rangle$ is coupled to optimization of the f_K expansion coefficients [32,49,50]. For a given $|\Phi\rangle$, the optimal f_K constitute the lowest-energy solution to the generalized eigenvalue problem for the Hamiltonian $\hat{H}$ in the nonorthogonal basis spanned by $\{\hat{P}_{MK}^S|\Phi\rangle\}$, $K = -S, -S+1, ..., +S$ [32,50]. For combined S and PG projection, the projector is a product, $\hat{P} = \hat{P}_M^S\hat{P}_\Gamma$ (spin rotations commute with PG operations). When working with the trivial group that contains only the identity operation, $\hat{P} = \hat{1}$, PHF becomes equivalent to HF.

For the optimization with respect to $|\Phi\rangle$, we adopted an SCF approach based on successively building and diago-

[1]The usual nonrelativistic Hamiltonians, including the Heisenberg spin model, are invariant under the product group $SU(2) \times T \times PG$, where $SU(2)$ corresponds to spin-rotational symmetry, T is the time-reversal group, and PG is the point group [37,96].

nalizing an effective Fock matrix [32,50]. An efficient SCF algorithm was recently developed for SGHF [50], and subsequently extended to KSGHF or PGKSGHF [43]. For the present spin problem, the density matrix is block diagonal in the local spin basis, with each block describing a pure state of a specific site spin. It is crucial to exploit this block structure, as explained in the detailed PGSGHF and PGKSGHF algorithms given in the SM.

In one previous very brief application of PHF to Heisenberg systems [51], SGHF spin-pair correlation functions for the $s = \frac{1}{2}$ AFH spin ring with $N = 24$ sites were reported, but the AFH represented only a side aspect of that work. The lack of size extensivity [32,35] (PHF recovers zero correlation energy per spin site in the thermodynamic limit, $N \to \infty$) becomes problematic for large systems. Post-PHF methods can ameliorate this problem, but such methods were not yet considered for spin Hamiltonians. Symmetry-projected configuration-mixing schemes [52] allow one to systematically approach exact ground and excited states and were applied to the 1D and 2D single-band Hubbard model [49,52–56]. Additional post-PHF methods are cited in Ref. [57]. We believe that the present paper could stimulate explorations of some of these more advanced techniques for the Heisenberg model.

VB formulation. The $s = \frac{1}{2}$ Heisenberg model is converted to the canonical-VB form by writing site-spin operators $\hat{\mathbf{s}}_i$ in terms of fermionic creation and annihilation operators (Abrikosov representation)

$$\hat{\mathbf{s}}_i = \frac{1}{2} \sum_{\alpha\beta} \hat{c}^\dagger_{i\alpha} (\boldsymbol{\sigma})_{\alpha\beta} \hat{c}_{i\beta}, \tag{6}$$

where $\alpha = \uparrow, \downarrow$ and $\beta = \uparrow, \downarrow$ (α and β are usually called flavor indices), and $\boldsymbol{\sigma}$ is the set of Pauli matrices, $\boldsymbol{\sigma} = (\boldsymbol{\sigma}_x, \boldsymbol{\sigma}_y, \boldsymbol{\sigma}_z)^T$. When written in terms of Eq. (6), the Hamiltonian, Eq. (7), is defined on the much larger state-space of the single-band Hubbard model.

$$\begin{aligned} \hat{H} = & \frac{1}{2} \sum_{i<j} J_{ij} (\hat{c}^\dagger_{i\uparrow} \hat{c}^\dagger_{j\downarrow} \hat{c}_{j\uparrow} \hat{c}_{i\downarrow} + \text{H.c.}) \\ & + \frac{1}{4} \sum_{i<j} J_{ij} (\hat{c}^\dagger_{i\uparrow} \hat{c}_{i\uparrow} - \hat{c}^\dagger_{i\downarrow} \hat{c}_{i\downarrow})(\hat{c}^\dagger_{j\uparrow} \hat{c}_{j\uparrow} - \hat{c}^\dagger_{j\downarrow} \hat{c}_{j\downarrow}). \end{aligned} \tag{7}$$

The physical constraint that every site hosts exactly one fermion can be formally enforced through the Gutzwiller projector, $\hat{P}_\text{G} = \prod_i (\hat{1} - \hat{c}^\dagger_{i\uparrow} \hat{c}_{i\uparrow} \hat{c}^\dagger_{i\downarrow} \hat{c}_{i\downarrow})$. In HF solutions for extended 2D or 3D systems, single occupancy generally holds on average only, $\sum_\alpha \langle \hat{c}^\dagger_{i\alpha} \hat{c}_{i\alpha} \rangle = 1$, meaning that ionic states contribute some weight. In PHF, we can completely avoid ionic states by exploiting the block structure of the single-particle density matrix, see the SM. This also makes calculations far more efficient compared to working in the full state space of the corresponding Hubbard model. A Slater determinant $|\Phi\rangle$ with exact single occupation obviously represents a 3D spin configuration of the $s = \frac{1}{2}$ system.

For $s > \frac{1}{2}$ we introduce a single fermion (SF) per site, with flavor multiplicity $2s + 1$, by generalizing Eq. (6) to Eq. (8) [58–60],

$$\hat{\mathbf{s}}_i = \sum_{\alpha\beta} \hat{c}^\dagger_{i\alpha} (\boldsymbol{\tau})_{\alpha\beta} \hat{c}_{i\beta}, \tag{8}$$

where $\boldsymbol{\tau} = (\boldsymbol{\tau}_x, \boldsymbol{\tau}_y, \boldsymbol{\tau}_z)^T$ are the spin matrices (for $s = \frac{1}{2}$, $\boldsymbol{\tau} = \frac{1}{2}\boldsymbol{\sigma}$). In the respective itinerant-fermion model, every site could, in principle, host up to $2s + 1$ fermions. However, as noted, the single-occupancy constraint is straightforwardly built into the PHF algorithm. Independent of the coupling topology or the local spin-quantum number s, the zero-field Hamiltonian contains only quartic interaction terms and no quadratic (hopping) contributions [$t_{lm} = 0$ in Eq. (1)]. Most interaction integrals $[kn|lm]$ are zero, where k, l, m, n are compound site and flavor indices. The total number of non-vanishing integrals increases with s.

In a closely related second option for fermionization, we introduce multiple fermions (MFs) per site, instead of just a single fermion (SF). In the MF approach, every site spin is formally decomposed into a number of $2s$ copies of spin-1/2 degrees of freedom,

$$\hat{\mathbf{s}}_i \to \sum_{\kappa=1}^{2s} \hat{\mathbf{s}}_{i\kappa}. \tag{9}$$

In common terminology [61], $n_c = 2s$ is the color number, and κ is a color index. When written in terms of spin-1/2 couplings (cf. Eq. (19) in Ref. [61]),

$$\hat{H} = \sum_{i<j} J_{ij} \hat{\mathbf{s}}_i \cdot \hat{\mathbf{s}}_j \to \sum_{i<j} J_{ij} \left(\sum_\kappa \hat{\mathbf{s}}_{i\kappa} \right) \cdot \left(\sum_{\kappa'} \hat{\mathbf{s}}_{j\kappa'} \right), \tag{10}$$

the Hamiltonian extends the Hilbert space, because the spin-1/2 sites can couple to different values of the local spin. However, this does not pose a practical problem in PHF, because each site can be easily enforced to have its maximal spin s (see the SM). Fermionization of Eq. (10) according to Eq. (6) yields the MF representation. Defining an orbital in terms of a combination $i\kappa$ of a site and a color index, MF is the strong-coupling limit of the half-filled Hubbard model with $n_c = 2s$ orbitals per site [62].

There is a qualitative difference between SF and MF. In MF, a mean-field state $|\Phi\rangle$ which fulfills the physical constraint of maximal local spin s corresponds to a spin-coherent product state. In other words, $|\Phi\rangle$ is a spin configuration. A

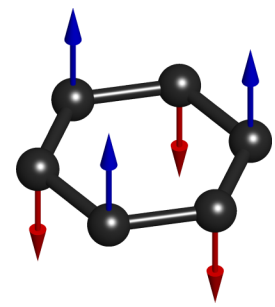

FIG. 1. RBM corresponds to projecting the Néel configuration (the HF solution, with blue/red spins pointing up/down) onto the different spin sectors, $0 \leqslant S \leqslant Ns$. The Néel configuration is not optimal for spin projection (except for $S = Ns$), cf. Fig. 2.

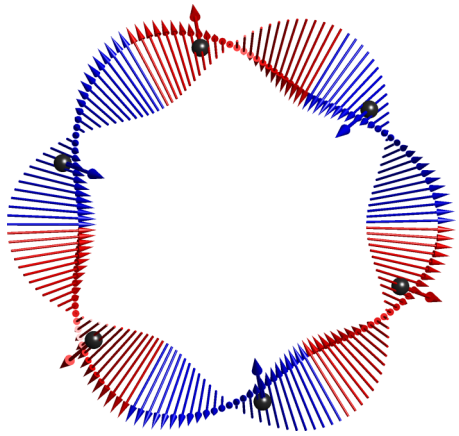

FIG. 2. The SGHF ($S = 0$) reference state $|\Phi\rangle$ adopts a three-dimensional Möbius-type configuration for $N = 6$, $s = \frac{1}{2}$, see vectors attached to spin sites (marked by spheres). A Möbius band with six twists is illustrated in terms of a set of vectors around the circle (thin arrows are drawn for illustration only), seen from the positive z axis. Blue/red vectors point in the positive/negative z direction. $|\Phi\rangle$ is symmetric under $\hat{\Theta} \times \exp(-i\frac{2\pi}{6}\hat{S}_z) \times \hat{C}_6$, where the time-reversal operation $\hat{\Theta}$ flips all spins.

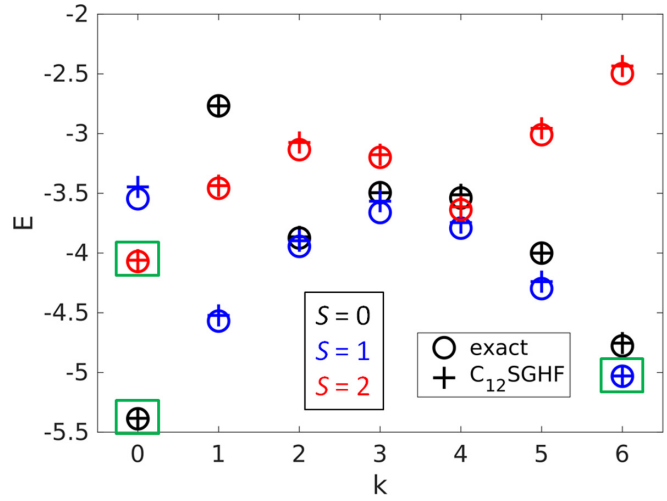

FIG. 3. Energies of the lowest levels with total spin $S = 0$ (black), $S = 1$ (blue), and $S = 2$ (red), in different k sectors of the $N = 12$, $s = \frac{1}{2}$ AFH ring, calculated exactly (O symbols) or by C_{12}SGHF (+ symbols). Numerical values are collected in Table I. Three levels belonging to the lowest rotational band are highlighted (green boxes).

noncoplanar (3D) spin configuration completely breaks S and K symmetry and is defined by $2N$ real parameters, where a pair of polar angles (ϑ, φ) specifies the orientation of each maximally polarized site spin. On the other hand, in SF, $|\Phi\rangle$ is a general product state of local spin-wave functions, which has $4sN$ independent degrees of freedom. [A state of a single spin is specified by $(2s + 1)$ complex numbers, but normalization and factoring out a phase reduce this to $4s$ real parameters.] In summary, SF does not constrain $|\Phi\rangle$ to be a spin-coherent product state. Therefore, SF grants more variational freedom than MF, and PHF based on SF generally affords lower energies. Unless noted otherwise, all our PHF results refer to the SF representation. The Jordan-Wigner (JW) transformation may come to mind as an alternative fermionization scheme. However, it is basically limited to $s = \frac{1}{2}$ systems, and couplings must not reach beyond next-nearest neighbors, because the existing PHF equations permit only quadratic and quartic terms in the Hamiltonian; longer-range interactions would introduce sextic or higher-order terms in JW. Besides, PHF based on the JW representation must work in a definite S_z sector. That is, the number of JW fermions is fixed, and restoration of spin-symmetry is not straightforward. In these respects, the SF and MF representations are far more flexible, because they are not constrained with respect to coupling topology, spin-quantum number s, or symmetries. We indeed implemented PHF with PG and K restoration based on the JW transformation, but no results shall be presented.

Point-group (PG) symmetry. The high symmetry of many molecular spin clusters manifests as PG symmetry of the spin Hamiltonian [63–65]. For isotropic Hamiltonians, which are our only concern here, PG symmetry is associated with invariance under site permutations, which is sometimes called spin-permutational symmetry (SPS) [63]. Block diagonalization with respect to the PG species and the $\hat{S}_z$ eigenvalue is technically simple and facilitates ED [63,66,67]. Combining PG with full spin symmetry ($\hat{\mathbf{S}}^2$ and $\hat{S}_z$) is more involved [63,68,69]. Conversely, simultaneous PG and spin adaptation is very simple in PHF. A high molecular symmetry is indeed favorable for PHF, because breaking and restoring PG symmetry improves energies, and a larger number of states can be targeted. When aiming for excited states in the respective symmetry sectors, one should look towards

TABLE I. Exact (ED) and C_{12}SGHF energies for the lowest $S = 0$, $S = 1$ and $S = 2$ states in the different k sectors of the AFH $N = 12$, $s = \frac{1}{2}$ spin ring.[a]

S	k	0	1	2	3	4	5	6
0	ED	–5.3874	–2.7682	–3.8742	–3.4949	–3.5389	–4.0006	–4.7774
	C_{12}SGHF	–5.3831	–2.7682[b]	–3.8648	–3.4949[b]	–3.5129	–4.0006[b]	–4.7539
1	ED	–3.5457	–4.5694	–3.9443	–3.6608	–3.7914	–4.2977	–5.0315
	C_{12}SGHF	–3.4463	–4.5222	–3.8972	–3.5661	–3.7453	–4.2395	–5.0287
2	ED	–4.0705	–3.4577	–3.1349	–3.1989	–3.6374	–3.0097	–2.4983
	C_{12}SGHF	–4.0595	–3.4358	–3.0746	–3.1770	–3.6138	–2.9561	–2.4345

[a]Except for $k = 0$ and $k = 6$, pairs of k values are degenerate, $k = (1, 11)$, $k = (2, 9)$, etc. Only one k component of each pair is listed.
[b]C_{12}SGHF and ED agree within numerical double precision.

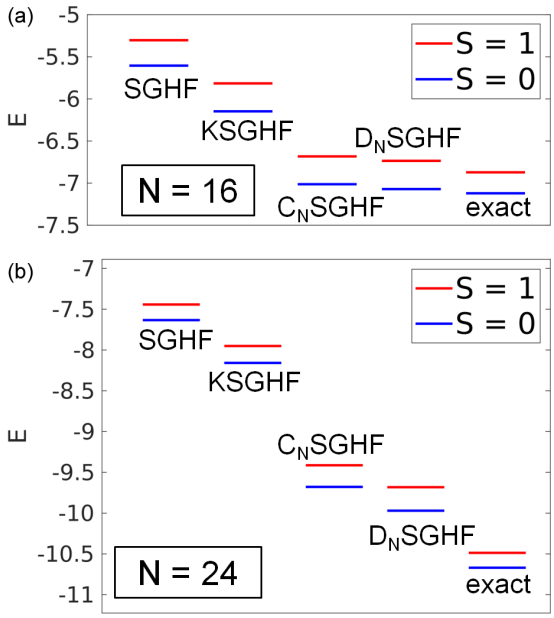

FIG. 4. Energy level diagrams for $s = \frac{1}{2}$ AFH rings with $N = 16$ (a) and $N = 24$ (b). Different variants of PHF are compared to exact energies for the lowest $S = 0$ and $S = 1$ levels.

multi-configuration post-PHF methods, which are beyond the scope of this paper.

Spin and fermionic representations generally do not agree on the attribution of PG-symmetry labels to specific states. All PG labels in the Results section refer to the spin representation. See Sec. 3 of the SM for further comments on this technical issue.

Computations. Calculations were carried out with an independently written program that essentially follows an efficient SGHF algorithm [50], which was recently extended to KS-GHF [43]. For applications to the Heisenberg model, it is crucial to exploit the block structure of the single-particle density matrix, as explained in Secs. 1 and 2 of the SM. SCF convergence requires a significant damping factor, applied at the level of effective Fock matrices. We generally found the commutator direct-inversion in the iterative subspace (c-DIIS) technique [70] to accelerate convergence in the later iteration stages. Several results were checked against an independent program that employs gradient-based optimization of the Thouless parameters that define the mean-field reference [71]. However, K-symmetry restoration or the MF option are not supported by the latter program. Transfer operators for spin projection [Eq. (5)] were discretized with a combined Lebedev-Laikov [72] and trapezoid integration grid [50]. The remaining error in $\langle \hat{\mathbf{S}}^2 \rangle$ was $<10^{-6}$, where $\langle \hat{\mathbf{S}}^2 \rangle$ is obtained by summing up spin-correlation functions $\langle \hat{\mathbf{s}}_i \cdot \hat{\mathbf{s}}_j \rangle$(SPCFs),

$$\langle \hat{\mathbf{S}}^2 \rangle = Ns(s+1) + 2 \sum_{i<j} \langle \hat{\mathbf{s}}_i \cdot \hat{\mathbf{s}}_j \rangle. \tag{11}$$

Compared to *ab initio* calculations on systems with a similar number of single-particle basis functions, larger integration grids are needed for the Heisenberg model, because all particles (spins) are part of the static-correlation problem, whereas in molecular HF wave functions, most electrons are approximately singlet paired. In our experience, the size of the spin-projection grid required for comparable accuracy across different systems grows only weakly (sublinearly) with system size. Note that a computational parallelization of the summation over the grid is trivial [50]. The calculation of SPCFs is analogous to the evaluation of the energy of the projected state [cf. Eq. (2)]. A double integration over the spin-projection grid can be trivially avoided, because $\hat{\mathbf{s}}_i \cdot \hat{\mathbf{s}}_j$ is a spin scalar which commutes with the (Hermitian and idempotent) spin-projection operator, see Eq. (13) below. For PG projection, we consider only 1D representations Γ. Then only the totally symmetric part $(\hat{\mathbf{s}}_i \cdot \hat{\mathbf{s}}_j)_{\Gamma_1}$, Eq. (12),

$$(\hat{\mathbf{s}}_i \cdot \hat{\mathbf{s}}_j)_{\Gamma_1} = \frac{1}{h} \sum_{g=1}^{h} \hat{G}^\dagger(g) (\hat{\mathbf{s}}_i \cdot \hat{\mathbf{s}}_j) \hat{G}(g), \tag{12}$$

contributes to $\langle \Phi | \hat{P}^\dagger_\Gamma (\hat{\mathbf{s}}_i \cdot \hat{\mathbf{s}}_j) \hat{P}_\Gamma | \Phi \rangle$. Overall, a single summation/integration is required to evaluate SPCFs for PGSGHF wave functions,

$$\langle \Phi | \hat{P}^\dagger_S \hat{P}^\dagger_\Gamma (\hat{\mathbf{s}}_i \cdot \hat{\mathbf{s}}_j) \hat{P}_S \hat{P}_\Gamma | \Phi \rangle = \langle \Phi | (\hat{\mathbf{s}}_i \cdot \hat{\mathbf{s}}_j)_{\Gamma_1} \hat{P}_S \hat{P}_\Gamma | \Phi \rangle. \tag{13}$$

In a slightly more complicated way, a double integration can also be avoided for spin densities $\langle \hat{\mathbf{s}}_i \rangle$, that is, expectation values of rank-1 operators [43,71], but spin densities are of no explicit concern here.

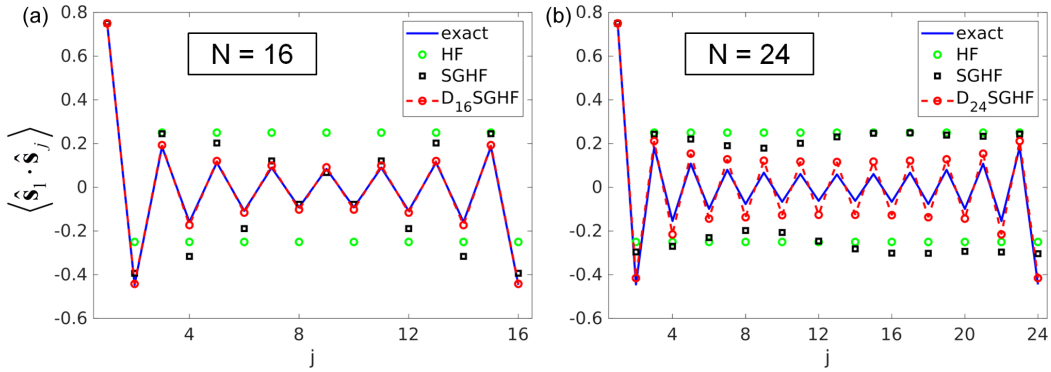

FIG. 5. Ground state ($S = 0$) SPCFs with respect to site 1 in $s = \frac{1}{2}$ AFH rings, for $N = 16$ (a) and $N = 24$ (b). HF, SGHF and D_NSGHF are compared to exact results. HF corresponds to the trivial Néel state, where SPCFs alternate between $\pm\frac{1}{2}$.

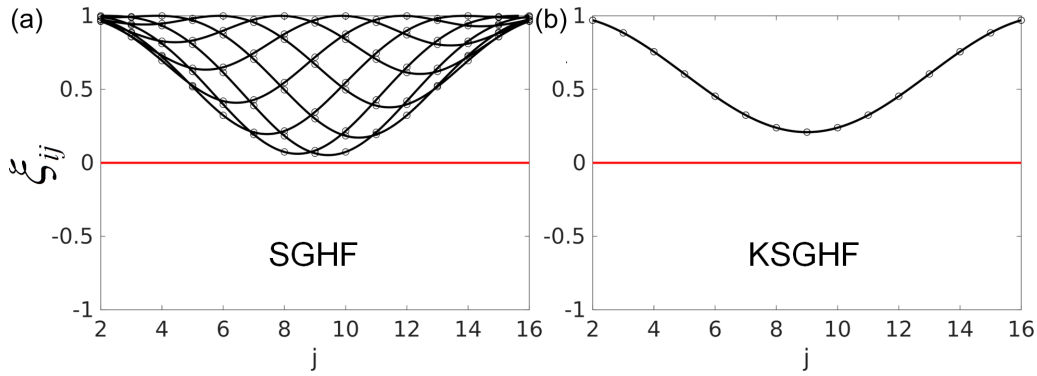

FIG. 6. Antiferromagnetic correlations ξ_{ij} [Eq. (16)] in the reference mean-field states for SGHF and KSGHF ($S = 0$), for the $N = 16$, $s = \frac{1}{2}$ ring. Each site is successively given the number $i = 1$ and ξ_{1j} is plotted for $j = 2, ..., 16$ (data points are connected by lines to guide the eye). Many points coincide in SGHF. Due to the Möbius structure (see Fig. 7) of the KSGHF solution $|\Phi\rangle$, the KSGHF curves are independent of the choice of the reference site. We optimized $\langle\Phi|\hat{H}|\Phi\rangle$ with respect to the allowed gauge transformations, see main text.

The relative correlation energy $0 \leqslant p \leqslant 1$ for PHF is defined in Eq. (14),

$$p = \frac{E_{\mathrm{PHF}} - E_{\mathrm{HF}}}{E_{\mathrm{ex}} - E_{\mathrm{HF}}}, \tag{14}$$

where E_{ex} is the exact energy ($E_{\mathrm{ex}} - E_{\mathrm{HF}}$ is the correlation energy). HF is equivalent to finding the optimal classical spin configuration and always yields a multispin coherent state. That is, SF is equivalent to MF for HF. (However, if biquadratic exchange or single-ion anisotropy terms were included in the spin Hamiltonian, SF could yield a lower-energy HF solution than MF.) Where no references for (Lanczos) ED results are given in the text, calculations were carried out with our own program which block factorizes the Hamiltonian with respect to the $\hat{S}_z$ eigenvalue and the SPS symmetry species. Unless noted otherwise, our benchmark systems have a nondegenerate $S = 0$ ground state. We denote the numerically exact ground-state energy by E_0. All energies are reported in units of the uniform nearest-neighbor coupling constant J.

III. RESULTS AND DISCUSSION

We consider the AFH for spin rings with a variable number N of centers, mainly for even N, with $\frac{1}{2} \leqslant s \leqslant \frac{7}{2}$, and for three polyhedra: truncated tetrahedron, icosahedron, and dodecahedron. The main objective is to provide PHF benchmark results for ground-state energies and SPCFs, where we compare against ED or DMRG results.

Spin rings. Early numerical studies of spin chains or rings were largely motivated by extrapolating singlet-triplet gaps, SPCFs, and other properties to the thermodynamic limit, see, e.g., Refs. [73–76]. More recent synthetic realizations of diverse ring-shaped spin clusters, followed by detailed investigations of their magnetic properties have added to the relevance of the Heisenberg model for rings of finite size (see Ref. [77] for a review).

Classically, AFH rings adopt a Néel configuration for even N, and coplanar helical configurations for odd N [78]. For even N, spin-projected PHF is closely related to the RBM, where we refer to the lowest rotational band only. In the RBM Hamiltonian, $\hat{H}_{\mathrm{RBM}} = j\hat{\mathbf{S}}_A \cdot \hat{\mathbf{S}}_B$, two composite spins $\hat{\mathbf{S}}_A = \sum_{i=\mathrm{odd}} \hat{\mathbf{s}}_i$ and $\hat{\mathbf{S}}_B = \sum_{i=\mathrm{even}} \hat{\mathbf{s}}_i$ ($S_A = S_B = Ns/2$) interact through an effective coupling constant j [17,79]. The RBM eigenstates are projections of the Néel configuration $|M_A = S_A, M_B = -S_B\rangle$ onto the different spin sectors, $0 \leqslant S \leqslant S_A + S_B$ [80]; a Néel configuration is illustrated in Fig. 1. RBM is thus equivalent to PAV-SGHF, where PAV stands for projection-after-variation. (The Néel state conserves $\hat{S}_z$ symmetry, so PAV-SGHF could be specialized to PAV-SUHF.) When $j = 4J/N$ is chosen to match the exact energy of the ferromagnetic $S = S_A + S_B$ state, then RBM and PAV-SGHF energies agree for all S, Eq. (15):

$$E_{\mathrm{RBM}} = \frac{j}{2}\left[S(S+1) - 2\frac{sN}{2}\left(\frac{sN}{2} + 1\right)\right]. \tag{15}$$

For three-colorable lattices [81], RBM and PAV-SGHF remain equivalent, see, e.g., the icosidodecahedron [17,18], and models for the triangular or Kagomé spin lattices [80]. However, PHF is a VAP approach. The classical (HF) solution is usually not optimal for spin projection, meaning that VAP will yield lower energies than PAV. An example is shown in Fig. 2: the optimal SGHF ($S = 0$) reference configuration for $N = 6$, $s = \frac{1}{2}$ is a 3D Möbius structure ($E_{\mathrm{RBM}} = -2.5$, $E_{\mathrm{SGHF}} = -2.7073$). Note that this regular

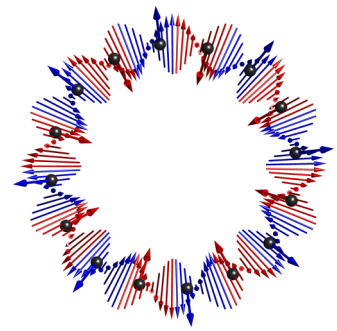

FIG. 7. Gauge-optimized spin configuration $|\Phi\rangle$ for combined K and S projection (KSGHF, $S = 0$) in an $N = 16$, $s = \frac{1}{2}$ ring. For more details, see caption to Fig. 2 and main text. $|\Phi\rangle$ is symmetric under $\hat{\Theta} \times \exp(-i\frac{2\pi}{16}\hat{S}_z) \times \hat{C}_{16}$.

TABLE II. Symmetry labels for D_NSGHF projection for the lowest $S = 0$ and $S = 1$ levels (Table III and Table IV) of AFH spin rings with $N = 4n$ or $N = 4n + 2$ sites, with $\frac{1}{2} \leqslant s \leqslant \frac{7}{2}$.

	$N = 4n+2$		$N = 4n$	
	$S=0$	$S=1$	$S=0$	$S=1$
1/2	B_2	A_1	A_1	B_2
1	A_1	B_2	A_1	B_2
3/2	B_2	A_1	A_1	B_2
2	A_1	B_2	A_1	B_2
5/2	B_2	A_1	A_1	B_2
3	A_1	B_2	A_1	B_2
7/2	B_2	A_1	A_1	B_2

structure was revealed through a global minimization of the energy expectation value $\langle\Phi|\hat{H}|\Phi\rangle$ with respect to the allowed gauge transformations (local spin rotations). Specifically, due to a nontrivial redundancy with respect to nonunitary gauge transformations of $|\Phi\rangle$, a continuum of nondegenerate mean-field states yields the same state upon S projection [82]. C_6SGHF yields the exact ($S = 0, k = 3$) ground state ($E_0 = -2.8028$) within numerical double precision (k specifies the eigenvalue $e^{ik2\pi/N}$ of the cyclic spin-permutation operator $\hat{C}_N$). The C_6SGHF solution $|\Phi\rangle$ is different from the SGHF solution.

The polyhedra discussed below have 3D (noncoplanar) HF solutions (GHF). We found a number of cases where the GHF solution also constituted an SGHF or KSGHF solution. However, in all cases considered, a VAP scheme yields lower energies than PAV when PG projection is introduced.

We resume our discussion of $s = \frac{1}{2}$ rings by briefly noting that KGHF offers little advantage over HF. Spin configurations which are not xz coplanar, break K symmetry [37,83], where $\hat{K}_0 = \hat{\Theta} \times \exp(-i\pi\hat{S}_y)$ is the operator of complex conjugation, and $\hat{\Theta}$ is the time-reversal operator (however, to break K symmetry irrespective of angular-momentum phase conventions or the orientation of the coordinate system, the spin configuration must not be confined to *any* plane). Restoration of K symmetry in KGHF yields an xz-coplanar state, which is a superposition of $|\Phi\rangle$ and $|\Phi^*\rangle$, where complex conjugation refers to the local spin basis, cf. the CMO method [45]. For an $N = 3$ spin ring, KGHF is exact for the $S = \frac{1}{2}$ ground state, yielding $E_0 = -\frac{3}{4}$. In the KGHF wave function, $\hat{\mathbf{s}}_1$ and $\hat{\mathbf{s}}_2$ are coupled to zero spin, $S_{12} = 0$, leaving a free (unentangled) $\hat{\mathbf{s}}_3$, whose orientation in the xz plane is

TABLE IV. Singlet-triplet gaps ΔE_{ST} in AFH rings with variable N and s. D_NSGHF energies are compared to exact or DMRG energies.[a]

	N					
s	6	12	18	24	30	Method
1/2	0.685	0.356	0.241	0.183	0.147	Exact
	0.685	0.355	0.331	0.286	0.212	PHF
1	0.721	0.484	0.432	0.417	0.413	Exact/DMRG
	0.721	0.455	0.298	0.213	0.165	PHF
3/2	0.705	0.407	0.300	0.242	0.205	Exact/DMRG
	0.705	0.412	0.269	0.195	0.152	PHF
2	0.697	0.391	0.284	0.229	0.195	Exact/DMRG
	0.697	0.381	0.256	0.188	0.147	PHF
5/2	0.692	0.378	0.268	0.211	0.176	Exact/DMRG
	0.692	0.381	0.286	0.184	0.145	PHF
3	0.688	0.370	0.259	0.202	0.167	Exact/DMRG
	0.688	0.374	0.245	0.181	0.143	PHF
7/2	0.685	0.364	0.253	0.196	0.161	Exact/DMRG
	0.685	0.369	0.242	0.179	0.142	PHF

[a]See footnote to Table III on exact/DMRG data.

TABLE III. Energies of the $S = 0$ ground state of AFH rings with variable N and s. D_NSGHF energies are compared to exact or DMRG energies.[a]

	N					
s	6	12	18	24	30	Method
1/2	–2.803	–5.387	–8.023	–10.670	–13.322	exact
	–2.803	–5.387	–7.851	–9.970	–11.814	PHF
1	–8.617	–16.870	–25.242	–33.641	–42.046	Exact/DMRG
	–8.617	–16.738	–24.252	–31.172	–37.833	PHF
3/2	–17.393	–34.131	–51.031	–67.968	–84.919	Exact/DMRG
	–17.393	–33.935	–49.580	–64.442	–78.934	PHF
2	–29.165	–57.408	–85.873	–114.390	–142.927	Exact/DMRG
	–29.165	–57.128	–83.919	–109.726	–135.048	PHF
5/2	–43.935	–86.679	–129.703	–172.793	–215.909	Exact/DMRG
	–43.934	–86.321	–127.263	–167.014	–206.166	PHF
3	–61.704	–121.948	–182.532	–243.197	–303.893	Exact/DMRG
	–61.704	–121.515	–179.610	–236.305	–292.286	PHF
7/2	–82.473	–163.217	–244.361	–325.601	–406.877	Exact/DMRG
	–82.473	–162.708	–240.957	–317.596	–393.407	PHF

[a]Where possible, we directly calculated exact (ED) energies or took them from the literature (Ref. [76]). Otherwise, DMRG energies were taken from Table V.1 in Ref. [86]. All the present ED/DMRG entries agree with the latter table. For the largest systems, the DMRG energies may not be accurate to all digits [86], but we expect such errors to be small compared to the errors in PHF.

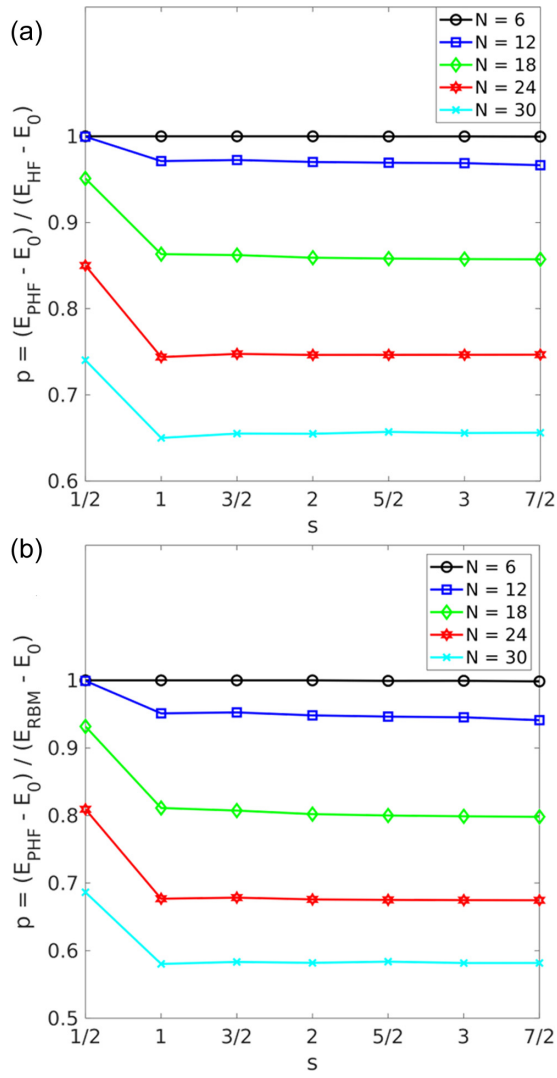

FIG. 8. Relative correlation energies p, with respect to HF (a) and RBM (b) captured by D_NSGHF in AFH rings with variable N and s. Data points are connected by lines to guide the eye. The ground-state energies from ED or DMRG (E_0) and D_NSGHF ($E_{\rm PHF}$) are collected in Table III; $E_{\rm HF} = -NJs^2$ and $E_{\rm RBM}$ is given in Eq. (15).

arbitrary. The lack of size consistency of PHF [32] can be illustrated for two noninteracting $N = 3$ rings where, obviously, $E_0 = -\frac{6}{4}$. KGHF yields a pure $S = 0$ state with a higher energy of $E = -\frac{5}{4}$. For $N = 4$, the KGHF solution is spin contaminated, $\langle \hat{\mathbf{S}}^2 \rangle \approx 1.172$, with $E = -\sqrt{2}$ (within numerical precision), compared to the exact $E_0 = -2$. The KGHF spin density shows Néel order for even N, $|\langle \Psi | \hat{\mathbf{s}}_i | \Psi \rangle| = (-1)^i g(N)$. The magnitude $g(N) < \frac{1}{2}$ of the sublattice magnetization is accessible from a simple formula given in Ref. [84]; $g(N)$ is the same for all sites for a given N. For large N, the KGHF correlation energy converges quickly onto a constant, $E_{\rm KGHF} - E_{\rm HF} \approx -0.366$ (for even N). A similar observation was made earlier in the Hubbard model [85].

On a qualitative note, in the molecular electronic-structure problem, K and S projection account mainly for dynamical and static correlation, respectively [32]. Our results below indeed show that S and PG symmetry are far more important than K symmetry. This is not surprising, because we are dealing with a prototypical static-correlation problem. The inclusion of K projection sometimes captures a significant fraction of the correlation energy missing from PGSGHF (see results below), but PGKSGHF was generally more difficult to converge, and most of our results refer to PGSGHF.

We discuss an $N = 12$, $s = \frac{1}{2}$ ring in some detail as an illustrative example. In Table I, C_{12}SGHF energies are compared to exact energies for $S = 0$, $S = 1$, and $S = 2$, in all k sectors. Energies are plotted in Fig. 3. We observe C_{12}SGHF to be numerically exact (with the double precision used in the calculations) for $S = 0$ in sectors $k = 1, 3, 5$. [It is worth noting in this context that it is somewhat nontrivial to predict in which (S, k) sectors C_{12}SGHF should converge onto the exact solution, see Sec. 4 of the SM.] Errors for the other $S = 0$ states are small. Although errors tend to be somewhat larger for $S = 1$ and $S = 2$, the levels $(S = 0, k = 0)$, $(S = 1, k = 6)$ and $(S = 2, k = 0)$ that belong to the lowest rotational band, are described with high precision by C_{12}SGHF.

For the global $(S = 0, k = 0)$ ground state, K projection fully captures the missing correlation energy, that is, C_{12}KSGHF is exact. The rather large errors of SGHF ($E = -4.5568$) and KSGHF ($E = -5.0208$) with respect to the exact $S = 0$ ground-state energy ($E_0 = -5.3874$) confirm the importance of combined S and PG projection. SGHF breaks

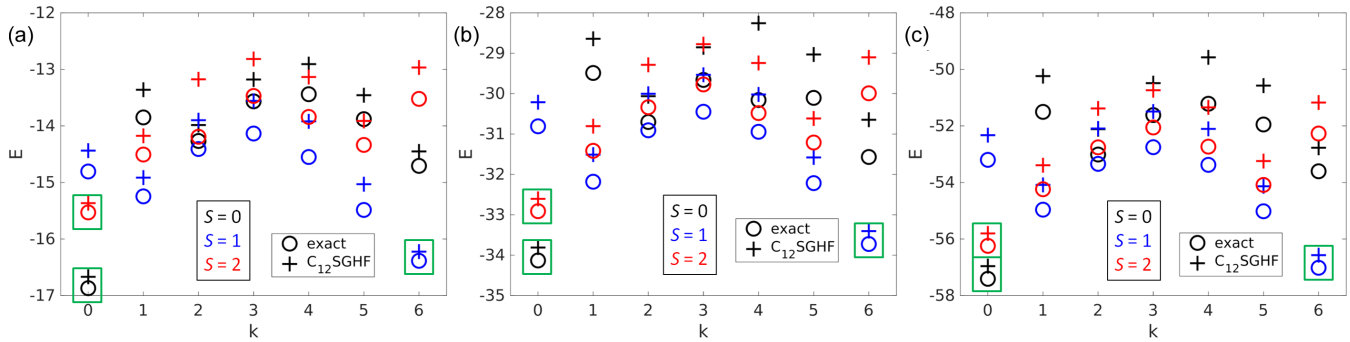

FIG. 9. Energies of the lowest levels with total spin $S = 0$ (black), $S = 1$ (blue), and $S = 2$ (red), in different k sectors of the $N = 12$ AFH ring with $s = 1$ (a), $s = \frac{3}{2}$ (b), and $s = 2$ (c), calculated exactly (O symbols) or by C_{12}SGHF (+ symbols). Three levels belonging to the lowest rotational band are highlighted in green boxes.

TABLE V. SPCFs in the $S = 0$ ground state of the $N = 12$ ring with $1 \leqslant s \leqslant 2$. D_NSGHF is compared to ED.[a]

	$s = 1$		$s = \frac{3}{2}$		$s = 2$	
	ED	PHF	ED	PHF	ED	PHF
$\langle \hat{\mathbf{s}}_1 \cdot \hat{\mathbf{s}}_2 \rangle$	–1.406	–1.395	–2.844	–2.828	–4.784	–4.761
$\langle \hat{\mathbf{s}}_1 \cdot \hat{\mathbf{s}}_3 \rangle$	0.778	0.820	1.913	1.976	3.535	3.634
$\langle \hat{\mathbf{s}}_1 \cdot \hat{\mathbf{s}}_4 \rangle$	–0.632	–0.722	–1.693	–1.828	–3.228	–3.438
$\langle \hat{\mathbf{s}}_1 \cdot \hat{\mathbf{s}}_5 \rangle$	0.504	0.597	1.490	1.615	2.940	3.142
$\langle \hat{\mathbf{s}}_1 \cdot \hat{\mathbf{s}}_6 \rangle$	–0.462	–0.574	–1.432	–1.570	–2.858	–3.078
$\langle \hat{\mathbf{s}}_1 \cdot \hat{\mathbf{s}}_7 \rangle$	0.436	0.544	1.384	1.518	2.788	3.003

[a]ED results from Ref. [75].

C_{12} symmetry, but $k = 0$ still dominates in the SGHF wave function, with a weight of $w_{k=0} = 0.85$.

The lack of size extensivity of PHF [32,35] means that the fractional correlation energy [Eq. (14)] tends to zero in the limit $N \to \infty$. For $s = \frac{1}{2}$ systems, this problem becomes apparent for ring sizes which are still straightforward for ED. As an illustration, we plot $S = 0$ and $S = 1$ energy levels for $N = 16$ and $N = 24$ in Fig. 4. D_{16}SGHF is still reasonably accurate (the singlet-triplet gap ΔE_{ST} is overestimated, though), but errors are significant for D_{24}SGHF.

As a measure of the quality of the wave functions, it is not surprising that SPCF predictions also deteriorate with increasing N. For $N = 16$ and $N = 24$, SPCFs from HF, SGHF and D_NSGHF are plotted against the exact results in Fig. 5. For $N = 16$, D_NSGHF is still reasonably accurate, but for $N = 24$ the magnitude of SPCFs is significantly overestimated. SPCFs from PHF approach long-range order for $N \to \infty$.

Although SGHF breaks cyclic symmetry, the correct representation of C_N contributes a dominant weight of $w_{k=0} = 82.8\%$ for $N = 16$ and $w_{k=0} = 79.7\%$ for $N = 24$. The broken C_{24}-symmetry in SGHF renders our present SPCF plot in Fig. 5 different from the respective plot in Fig. 15 of Ref. [51], due to a different choice of the $j = 1$ reference site. The choice of the reference site becomes irrelevant when cyclic symmetry is restored.

In applications of symmetry-projected quasiparticle methods to the single-band Hubbard model [54–56], the quantity ξ_{ij}, defined in Eq. (16),

$$\xi_{ij} = \frac{(-1)^{i-j}}{s^2} \langle \Phi | \hat{\mathbf{s}}_i | \Phi \rangle \cdot \langle \Phi | \hat{\mathbf{s}}_j | \Phi \rangle, \tag{16}$$

has proven qualitatively useful to show how $|\Phi\rangle$ differs from $|\Phi\rangle_{\mathrm{HF}}$. In Hubbard rings, $|\Phi\rangle$ was found to display antiferromagnetic defects, where $\xi_{ij} \approx 0$ and $\xi_{ij'} \approx 0$ (with a small distance between j and j') and $\xi_{ij''} < 0$ (for j'' lying between j and j'). Such defects, where the spin-density wave $|\Phi\rangle$ changes phase, were interpreted as basic units of quantum fluctuations [54].

In spin rings, correlations are perfectly antiferromagnetic in the Néel state, that is, $\xi_{ij} = 1$ for all $i \neq j$. For $N = 16$, we plot ξ_{ij} for SGHF and KSGHF ($S = 0$) in Fig. 6. The ξ_{ij} quantities are not uniquely determined, due to gauge freedom [82] in defining $|\Phi\rangle$. We thus performed a minimization of $\langle \Phi | \hat{H} | \Phi \rangle$ with respect to the allowed gauge transformations. In this way, a rather regular structure is revealed for SGHF [Fig. 6(a)] and a very regular Möbius structure for KSGHF [Figs. 6(b) and 7]. For KSGHF, ξ_{ij} depends only upon the distance $|i-j|$. SGHF and KSGHF are significantly in error with respect to the exact ground state energy (see Fig. 4) and do not display defects in their respective reference states, although correlations ξ_{ij} are significantly less antiferromagnetic than in HF. A number of $\xi_{ij} \approx 0$ and $\xi_{ij} < 0$ pairs occur for the more accurate methods C_{16}SGHF and C_{16}KSGHF (not shown).

Moving beyond $s = \frac{1}{2}$, we compare $S = 0$ ground-state energies from D_NSGHF to ED or DMRG in Table III, for $N = 6$, 12, 18, 24, 30, with $\frac{1}{2} \leqslant s \leqslant \frac{7}{2}$. Singlet-triplet gaps ΔE_{ST} are compared in Table IV. The D_N labels for PG projection onto the respective singlet and triplet states are collected in Table II.

For a given N, PHF captures larger fractions of E_0 with increasing s, but this is not a suitable accuracy measure, because even HF becomes exact in the classical limit $s \to \infty$. The relative correlation energy [Eq. (14)] measures the relative improvement over HF and remains roughly constant in the range $1 \leqslant s \leqslant \frac{7}{2}$, see Fig. 8(a). The same is true when measuring the performance against RBM by replacing E_{HF} in Eq. (14) by E_{RBM}, as shown in Fig. 8(b).

As a complement to Fig. 3 ($s = \frac{1}{2}$), C_{12}SGHF and ED energies for $S = 0$, $S = 1$, and $S = 2$ in all k sectors are compared for $1 \leqslant s \leqslant 2$ in Fig. 9. C_{12}SGHF and ED follow the same qualitative trend, but the errors from C_{12}SGHF are significantly larger than for $s = \frac{1}{2}$. The lowest rotational-band levels are again described with higher precision than other levels.

For $N = 12$, with $1 \leqslant s \leqslant 2$, SPCFs from D_{12}SGHF are compared to ED results in Table V and plotted in Fig. 10. Relative errors in the SPCFs from D_{12}SGHF decrease with

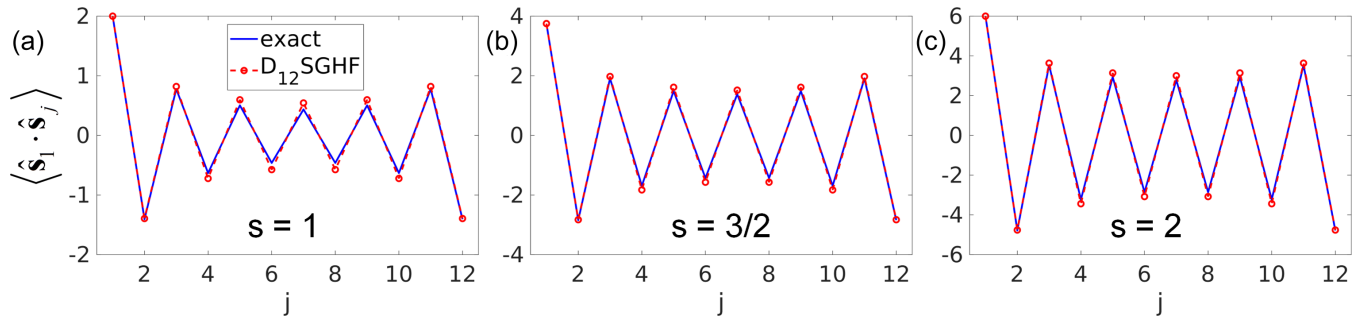

FIG. 10. Ground state ($S = 0$) SPCFs with respect to site 1, in the $N = 12$ AFH ring with $s = 1$ (a), $s = \frac{3}{2}$ (b) and $s = 2$ (c). D_NSGHF is compared to exact results.

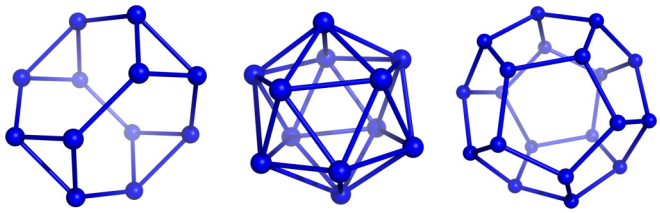

FIG. 11. Truncated tetrahedron, icosahedron, and dodecahedron (from left to right). Spheres represent spin sites. Connections between spheres mark antiferromagnetic interactions.

increasing s. SPCFs from PHF approach long-range order for $N \to \infty$.

The performance of PHF is put into perspective by regarding the size of the matrices that occur in ED. As an example, for $N = 12$, the full Hilbert space has a dimension of $\mathcal{N} = 5^{12} \approx 244 \times 10^6$ for $s = 2$ and $\mathcal{N} = 6^{12} \approx 2.2 \times 10^9$ for $s = \frac{5}{2}$. Although the subspaces with definite SPS and $\hat{S}_z$ symmetry are smaller by $\sim$ two orders of magnitude and thereby accessible to Lanczos ED, they are still huge compared to the number of variational parameters in PHF ($N_v < 4sN$, see comments above). In the SCF algorithm, the effective Fock matrix consists of $N = 12$ blocks. Each block is of dimension $(2s + 1) \times (2s + 1)$ in the SF representation, or 2×2 in the MF representation, see Sec. 1 of the SM. Thus, the formal cost of PHF has a rather weak dependence on s (we, however, observed that somewhat larger spin-projection grids are needed for larger s). The fact that D_{12}SGHF captures 99.5% and 99.3% of E_0 for $s = 2$ and $s = \frac{5}{2}$ overall evidences a very effective state-space reduction. For a subset of systems, we checked that the difference between SF and MF, and between C_N or D_N projection is comparably small. For example, for $N = 12$, $s = 2$, we obtain $E = -56.860$ with MF-D_{12}SGHF and $E = -57.128$ with SF-D_{12}SGHF, that is, 99.0% and 99.5% of $E_0 = -57.408$ (cf. Table III). On the other hand, MF-C_{12}SGHF and SF-C_{12}SGHF yield $E = -56.680$ and $E = -56.960$, respectively. PG projection is very important, as SF-SGHF predicts a far higher energy of $E = -53.898$, which is still lower than $E_{\mathrm{RBM}} = -52$. The difference between SGHF and RBM proves that the classical Néel state is not optimal for $S = 0$ projection.

PHF can be fairly accurate even for systems that are too large for ED. Specifically, for $N = 18$, $s = \frac{5}{2}$, which roughly represents an experimentally studied Fe_{18} molecule [11],

TABLE VI. Ground-state energy of the AFH on the truncated tetrahedron with $\frac{1}{2} \leqslant s \leqslant 2$, from ED, HF and different PHF variants.

S	Γ	Exact	HF	SGHF	KSGHF	T_dSGHF	T_dKSGHF
$\frac{1}{2}$	A_2	–5.7009	–3	–4.7069	–5.2803	–5.7009[a]	–5.7009[a]
1	A_1	–17.1955	–12	–15.3649	–15.6033	–16.9951	–17.1334
$\frac{3}{2}$	A_2	–34.6402	–27	–32.0210	–32.0567	–34.1406	–34.4453
2	A_1	–58.1140	–48	–54.6772	–54.6835	–57.4203	–57.6753

[a]PHF and ED agree within numerical precision.

D_{18}SGHF affords 98.1% of E_0 (from DMRG [11]). D_{18}SGHF predicts a reasonably accurate ΔE_{ST} (Table IV), which belongs to a transition observed in INS experiments [11]. Absolute errors in energies become rather large for $N \geqslant 24$ (see Table III), even for $s = \frac{7}{2}$. We note that the PHF singlet-triplet gaps are quite different from the exact results, which is somewhat disappointing. Each state is optimized independently in PHF and some states are more accurately described than others, that is, there is a limited opportunity for beneficial error cancellation. ΔE_{ST} are overestimated for $s = \frac{1}{2}$, but generally underestimated for $s > \frac{1}{2}$. Additional D_NSGHF calculations for $s = \frac{1}{2}$ and $s = 1$ for singlet-triplet gaps up to $N = 60$ (data not shown) indicate that PHF predicts $\Delta E_{\mathrm{ST}} \to 0$ in the limit $N \to \infty$, that is, PHF does not develop the Haldane gap $\Delta E \approx 0.41$ for $s = 1$. It indeed appears that all states belonging to the first rotational band become degenerate in PHF for $N \to \infty$, irrespective of s.

The good performance for large s suggests that PHF or post-PHF methods could be significantly more effective for the multiband Hubbard model than for the single-band Hubbard model, at least in the strong-coupling regime. Only the single-band model was thus far investigated with projected quasiparticle methods [49,53–56].

Spin polyhedra. The AFH for spins on the vertices of polyhedra has been discussed in the context of fullerenes [87,88]. An increasing number of successful synthetic realizations of polyhedral spin clusters has added relevance to such models, which are interesting from the perspective of geometric spin frustration and display a number of remarkable properties [89]. For example, field-dependent metastabilities of classical states of the icosahedron [90], dodecahedron [87],

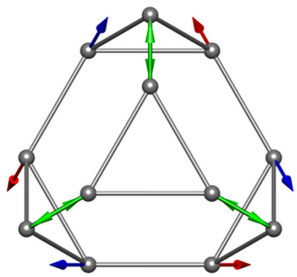

FIG. 12. Classical (GHF) solution of the AFH in the truncated tetrahedron (cf. Fig. 1 in Ref. [94]). Green arrows lie in the xy plane, blue/red arrows point in the positive/negative z direction.

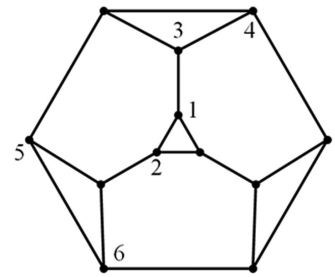

FIG. 13. Planar coupling graph of the truncated tetrahedron. Sites forming inequivalent pairs with site 1 are numbered to define SPCFs in Table VII.

TABLE VII. SPCFs for the $S = 0$ ground state of the truncated tetrahedron with $1 \leqslant s \leqslant 2$. Results from T_dSGHF are compared to exact values. The site numbers are defined in Fig. 13.[a]

	$s = 1$		$s = \frac{3}{2}$		$s = 2$	
	Exact	PHF	Exact	PHF	Exact	PHF
$\langle \hat{\mathbf{s}}_1 \cdot \hat{\mathbf{s}}_2 \rangle$	–0.6464	–0.6301	–1.3920	–1.3928	–2.3937	–2.3706
$\langle \hat{\mathbf{s}}_1 \cdot \hat{\mathbf{s}}_3 \rangle$	–1.5731	–1.5724	–2.9893	–2.9048	–4.8983	–4.8289
$\langle \hat{\mathbf{s}}_1 \cdot \hat{\mathbf{s}}_4 \rangle$	0.4499	0.4642	1.0235	1.0440	1.8381	1.8902
$\langle \hat{\mathbf{s}}_1 \cdot \hat{\mathbf{s}}_5 \rangle$	–0.4647	–0.5056	–1.0233	–1.0831	–1.8068	–1.9500
$\langle \hat{\mathbf{s}}_1 \cdot \hat{\mathbf{s}}_6 \rangle$	–0.0022	–0.0065	–0.0120	–0.0348	–0.0266	–0.0454

[a]Results for $s = \frac{1}{2}$ are not listed, because T_dSGHF is exact.

or truncated icosahedron [87] hint at unusual magnetization behavior in the respective quantum systems [87,91,92]. It was also discovered that the existence of independent-magnon states on certain spin polyhedra and the Kagomé lattice explain giant magnetization jumps towards saturation [93,94]. We here chose the truncated tetrahedron, the icosahedron, and the dodecahedron (Fig. 11) in order to briefly investigate the performance of PHF for systems with 2D coupling topologies. In each case, we consider only the $S = 0$ global ground state.

(i) Truncated tetrahedron

The classical solution $|\Phi_{\mathrm{HF}}\rangle$ for the AFH on the truncated tetrahedron minimizes frustration, with angles of 120° between neighboring spins on the four triangles, and antiparallel spins on intertriangle bonds [95] (see Fig. 12 below), yielding $E_{\mathrm{HF}} = -12s^2$. $|\Phi_{\mathrm{HF}}\rangle$ breaks SPS, but certain combinations of permutations and spin rotations leave $|\Phi_{\mathrm{HF}}\rangle$ unchanged. (We similarly found that $|\Phi_{\mathrm{HF}}\rangle$ for the truncated icosahedron [87] is invariant under combined permutations and spin rotations, where the symmetry axes of permutations and rotations do not coincide.) For $\frac{1}{2} \leqslant s \leqslant 2$, ground-state energies from different PHF variants are compared to ED in Table VI.

We first discuss the $s = \frac{1}{2}$ system, with a $^1A_2$ ground state in the T_d group. In Ref. [95], a trial state was constructed by $S = 0$ projection of $|\Phi_{\mathrm{HF}}\rangle$. This corresponds to PAV-SGHF, which we found constitutes also a VAP-SGHF solution. In other words, $|\Phi_{\mathrm{HF}}\rangle$ is an SGHF solution for $S = 0$, and also happens to be a KSGHF solution.

For all three polyhedra considered here, PAV-SGHF and VAP-SGHF turned out to be equivalent with respect to $S = 0$ projection for $\frac{1}{2} \leqslant s \leqslant \frac{5}{2}$ (we did not investigate larger s values). One could thus suspect that $|\Phi_{\mathrm{HF}}\rangle$ is optimal for a larger class of spin polyhedra, independent of s. For the icosahedron and dodecahedron this equivalence holds in representations SF and MF, but in the truncated tetrahedron, it is maintained only in MF, whereas SF yields lower energies. As an example, for the $s = 1$ truncated tetrahedron, SGHF predicts $E = -15.2879$ (MF) and $E = -15.3649$ (SF), and KSGHF yields $E = -15.5720$ (MF) and $E = -15.6033$ (SF).

SGHF affords a pure $^1A_2$ or $^1A_1$ term for $s = \frac{n}{2}$ or $s = n$, respectively, but it is not equivalent to T_dSGHF. However, $|\Phi_{\mathrm{HF}}\rangle$ must not constitute the initial guess for T_dSGHF, because it is apparently a local minimum (a rigorous classification of stationary states would require the PHF stability matrix [71], which is beyond the scope of this work). T_dSGHF yields the exact ground state for $s = \frac{1}{2}$, even when $|\Phi\rangle$ is constrained to be coplanar. For consistency, we also checked that SPCFs from T_dSGHF agreed with ED results. T_dKGHF does not implicitly restore spin symmetry, $\langle \hat{\mathbf{S}}^2 \rangle = 0.480$ ($E = -5.1447$), which contrasts with the $s = \frac{1}{2}$ icosahedron, where I_hKGHF converges onto the exact ground state (see below).

Coffey and Trugman [95] constructed another $s = \frac{1}{2}$ trial state by projecting a linear combination of $|\Phi_{\mathrm{HF}}\rangle$ and its time-reversed counterpart $\hat{\Theta}|\Phi_{\mathrm{HF}}\rangle$ onto the $S = 0$ sector, $|\Psi\rangle = a_1 \hat{P}_S |\Phi_{\mathrm{HF}}\rangle + a_2 \hat{P}_S \hat{\Theta} |\Phi_{\mathrm{HF}}\rangle$, where a_1 and a_2 were chosen to maximize overlap with the exact ground state ($|a_1|^2 + |a_2|^2 = 1$). This ansatz is similar to KSGHF, but yields a slightly lower energy. In a convention where energies are larger by a factor of four [95], this state has $E = -21.128$, while we obtain $E = -21.121$ with KSGHF.

For $s = 1$, $s = \frac{3}{2}$ and $s = 2$, T_dSGHF recovers 98.8%, 98.6% and 98.8% of E_0, respectively, which amounts to fractional correlation energies of $p = 96.1\%$, $p = 93.5\%$ and $p = 93.1\%$. K projection offers a further improvement, where T_dKSGHF yields $p = 98.8\%$, $p = 97.4\%$ and, $p = 95.7\%$,

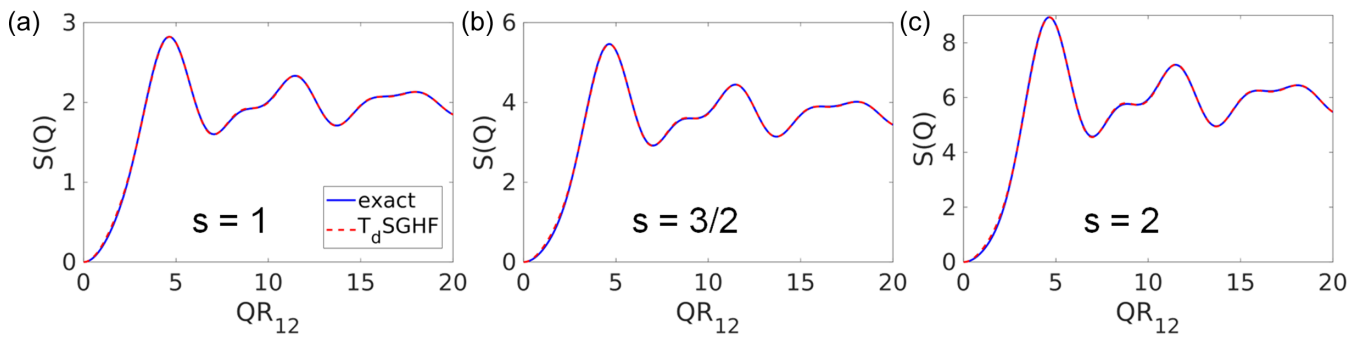

FIG. 14. Neutron-scattering structure factor $S(Q)$, Eq. (17), for the truncated tetrahedron. All edges are taken to have the same length R_{12}.

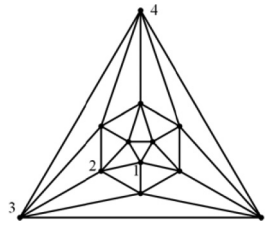

FIG. 15. Planar coupling graph for the icosahedron. Sites forming inequivalent pairs with site 1 are numbered.

respectively. The errors in SPCFs are similarly small, except for large relative errors for the most distant pair, $\langle \hat{\mathbf{s}}_1 \cdot \hat{\mathbf{s}}_6 \rangle$, see Table VII. The site numbers are defined in Fig. 13.

Following Ref. [95], the quality of SPCF predictions (Table VII) is illustrated by plotting the neutron-scattering structure factor $S(Q)$ for powder samples (ignoring form factors),

$$S(Q) = \frac{1}{N} \sum_{i,j} \langle \hat{\mathbf{s}}_i \cdot \hat{\mathbf{s}}_j \rangle j_0(QR_{ij}), \tag{17}$$

where $j_0(x) = \sin(x)/x$ is a spherical Bessel function and R_{ij} is the Cartesian distance between sites i and j. The exact and T_dSGHF curves $S(Q)$ for the $1 \leqslant s \leqslant 2$ systems are plotted in Fig. 14 and are almost indistinguishable.

(ii) Icosahedron

For the AHF on the icosahedron, with $\frac{1}{2} \leqslant s \leqslant 2$, the ground state alternates between $^1\mathrm{A_u}$ and $^1\mathrm{A_g}$ ($^1\mathrm{A_u}$ for $s = \frac{1}{2}$ [67], $^1\mathrm{A_g}$ for $s = 1$ [67], etc.). We note in passing that there are only four states in the $^1\mathrm{A_u}$ subspace for the $s = \frac{1}{2}$ system. With the help of symbolic computer algebra, we found an analytical expression for $E_0 \approx -6.1879$:

$$E_0 = -\frac{\sqrt{61}}{3}[\cos\alpha + \sqrt{3}\sin\alpha] - \frac{13}{6}, \tag{18}$$

where

$$\alpha = \frac{1}{3}\tan^{-1}\left(\frac{3\sqrt{19545}}{226}\right). \tag{19}$$

The classical (GHF) state also constitutes an SGHF ($S = 0$) solution in MF and SF representations. This implies that the SPS symmetry I is automatically restored (we, however, refrain from a detailed group-theoretical analysis). Consequently, symmetry-equivalent pairs have the same $\langle \hat{\mathbf{s}}_i \cdot \hat{\mathbf{s}}_j \rangle$. SGHF does not restore inversion symmetry C_i ($I_h = I \otimes C_i$), though. For $s = \frac{1}{2}$, the respective weights in the SGHF wave function are $w_{\mathrm{A_g}} = \frac{377}{622}$ and $w_{\mathrm{A_u}} = \frac{245}{622}$ ($w_{\mathrm{A_g}} + w_{\mathrm{A_u}} = 1$; the given fractions perfectly approximate the numerical values). An equal weight of $\mathrm{A_g}$ and $\mathrm{A_u}$ is quickly approached for larger s. Although I_hKGHF does not include explicit S projection, it remarkably converges onto the exact E_0 for $s = \frac{1}{2}$ (within double precision). I_hSGHF also yields the exact E_0, where, in contrast to I_hKGHF, $|\Phi\rangle$ may be constrained to be coplanar. We found an optimal coplanar $|\Phi\rangle$ with a peculiar pattern, where pairs of site spins are aligned antiparallel. Thus, one could implicitly define the exact ground state of the $s = \frac{1}{2}$ icosahedron by specifying $6-1 = 5$ angles for the relative orientation of the six spin-pairs in an arbitrary plane.

For the $s = 1$, $s = \frac{3}{2}$ and $s = 2$ systems, I_hSGHF (I_hKSGHF) recovers 99.90% (99.99%), 99.90% (99.97%), and 99.94% (99.97%) of E_0, respectively (cf. Table VIII), with small errors in SPCFs (site numbers are defined in Fig. 15), see Table IX.

(iii) Dodecahedron

The AFH ground state of the dodecahedron is $^1\mathrm{A_u}$ or $^1\mathrm{A_g}$ for $s = \frac{1}{2}$ or $s = 1$, respectively [67]. The classical solution $|\Phi_{\mathrm{HF}}\rangle$ [78,87] is invariant under combinations of permutations and uniform spin rotations that comprise a group isomorphic to I. [C_i must be combined with the time-reversal operation to leave $|\Phi_{\mathrm{HF}}\rangle$ unchanged, so the magnetic group [47] is $I_h(I)$.] We found that GHF is also an SGHF solution for $S = 0$ projection, in both SF and MF representations. SGHF implicitly restores I spin-permutational symmetry, but not C_i. For $s = \frac{1}{2}$, we find $w_{\mathrm{A_g}} \approx 0.516$ and $w_{\mathrm{A_u}} \approx 0.484$. Equal weights are approached for larger s. For $s = \frac{1}{2}$ and $s = 1$, I_hSGHF (I_hKSGHF) yields 98.5% (99.4%) and 96.4% (97.6%) of E_0, respectively, see Table X.

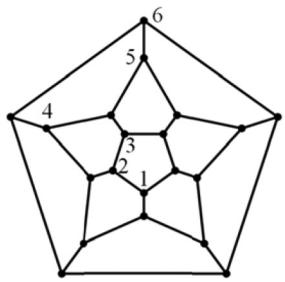

FIG. 16. Planar coupling graph for the dodecahedron. Sites forming inequivalent pairs with site 1 are numbered to define SPCFs in Table XI.

TABLE VIII. Ground-state energy of the AFH on the icosahedron with $\frac{1}{2} \leqslant s \leqslant 2$, from ED, HF, and different PHF variants.

s	Γ	Exact	HF[b]	SGHF	KSGHF	I_hSGHF	I_hKSGHF
$\frac{1}{2}$	$\mathrm{A_u}$	–6.1879	–3.3541	–5.2486	–5.8716	–6.1879[a]	–6.1879[a]
1	$\mathrm{A_g}$	–18.5611	–13.4164	–17.2992	–17.3990	–18.5419	–18.5596
$\frac{3}{2}$	$\mathrm{A_u}$	–37.7412	–30.1869	–36.0400	–36.0507	–37.7043	–37.7313
2	$\mathrm{A_g}$	–63.7104	–53.6656	–61.4853	–61.4862	–63.6713	–63.6915

[a]PHF is exact within numerical precision. [b]The HF energy is $E = -6\sqrt{5}s^2$ [78].

TABLE IX. SPCFs in the $S = 0$ ground state of the AFH on the icosahedron with $1 \leqslant s \leqslant 2$, from ED or I_hSGHF. The site numbers are defined in Fig. 15.[a]

	$s = 1$		$s = \frac{3}{2}$		$s = 2$	
	ED	PHF	ED	PHF	ED	PHF
$\langle \hat{\mathbf{s}}_1 \cdot \hat{\mathbf{s}}_2 \rangle$	–0.6187	–0.6181	–1.2580	–1.2568	–2.1237	–2.1224
$\langle \hat{\mathbf{s}}_1 \cdot \hat{\mathbf{s}}_3 \rangle$	0.3680	0.3702	0.9060	0.9134	1.6616	1.6706
$\langle \hat{\mathbf{s}}_1 \cdot \hat{\mathbf{s}}_4 \rangle$	–0.7463	–0.7608	–1.9899	–2.0331	–3.6897	–3.7411

[a]Results for $s = \frac{1}{2}$ are not listed, because I_hSGHF is exact.

TABLE X. Ground-state energy of the AFH on the dodecahedron with $s = \frac{1}{2}$ or $s = 1$, from ED, HF [95], and different PHF variants.

s	Exact	HF[a]	SGHF	KSGHF	I_hSGHF	I_hKSGHF
$\frac{1}{2}$	–9.7222	–5.5902	–7.3666	–7.4929	–9.5763	–9.6684
1	–30.2455	–22.3607	–25.8512	–25.8537	–29.1529	–29.5248

[a]The exact value is most likely $E = -10\sqrt{5}s^2$ [78].

We did not find the SPCFs for the $s = 1$ dodecahedron in the literature and the system is too large for our ED code. Therefore, Table XI compares SPCFs from PHF to ED results only for the $s = \frac{1}{2}$ system. The relative error in the $\langle \hat{\mathbf{s}}_i \cdot \hat{\mathbf{s}}_j \rangle$ tends to increase with increasing distance (site numbers are defined in Fig. 16), with an error of 28% for diametrically opposite sites, $\langle \hat{\mathbf{s}}_1 \cdot \hat{\mathbf{s}}_6 \rangle$. All SPCFs from I_hSGHF have the correct sign.

TABLE XI. SPCFs in the $S = 0$ ground state of the AFH on the $s = \frac{1}{2}$ dodecahedron, from ED or I_hSGHF. The site numbers are defined in Fig. 16.

	Exact	PHF
$\langle \hat{\mathbf{s}}_1 \cdot \hat{\mathbf{s}}_2 \rangle$	–0.3241	–0.3192
$\langle \hat{\mathbf{s}}_1 \cdot \hat{\mathbf{s}}_3 \rangle$	0.0654	0.0676
$\langle \hat{\mathbf{s}}_1 \cdot \hat{\mathbf{s}}_4 \rangle$	–0.0388	–0.0466
$\langle \hat{\mathbf{s}}_1 \cdot \hat{\mathbf{s}}_5 \rangle$	0.0331	0.0429
$\langle \hat{\mathbf{s}}_1 \cdot \hat{\mathbf{s}}_6 \rangle$	–0.0365	–0.0468

IV. SUMMARY AND OUTLOOK

We have investigated PHF theory as a simple black-box approximation for ground states of Heisenberg spin clusters. PHF yields states with definite spin- and point-group symmetry at a mean-field cost. Detailed equations for an SCF-type optimization are provided in the Supplemental Material. A fermionic formulation establishes a conceptual connection to electronic-structure theory, but unphysical ionic states can be excluded by construction, thereby substantially reducing the computational effort compared to the Hubbard model. The mean-field reference state can be chosen as either a spin-coherent state or a general multispin product state. The latter more flexible option affords lower variational energies. The compact wave-function representation in terms of a projection operator acting on a multispin product state is convenient and conceptually appealing.

Antiferromagnetic spin rings and polyhedra were chosen as suitable benchmark systems for comparing energies and spin-pair correlations from PHF against exact (or DMRG) results. With regard to capturing a large fraction of the ground-state energy, PHF is most problematic for small s. Combined S and PG projection produces exact eigenstates of $s = \frac{1}{2}$ spin rings with up to $N \approx 12$ sites, but the accuracy of PHF decreases sharply for larger N, signaling that the method is not suitable for investigating the thermodynamic limit.

PHF becomes far more accurate for larger s. For $s \geqslant 1$ the relative improvement over a classical (HF) treatment is approximately constant (independent of s). For example, for an $N = 18$ ring with $s = \frac{5}{2}$, PHF recovers ∼98% of the DMRG ground-state energy and predicts a reasonable singlet-triplet gap. Thus, PHF could be of practical use, e.g., for the simulation of INS excitations in molecular spin clusters. Our study of three spin polyhedra additionally showed that PHF works similarly well for 2D systems, which are less favorable for DMRG. These results indicate that PHF could be a useful complementary method for ground states of a wider class of high-symmetry spin clusters, particularly for large s and moderately large N.

A few aspects were not in the scope of this work. For example, systems with nonuniform s do not pose a difficulty but were not studied here. We also note that low-temperature spectroscopic properties, e.g., from magnetic-resonance experiments, could be modeled based on a first-order treatment of local Zeeman, hyperfine or zero-field splitting tensors. The required rank-1 or rank-2 spin-projection coefficients [1], can be straightforwardly calculated from the PHF single-particle or two-particle density matrices. For the calculation of INS intensities, single-particle transition-density matrices are needed.

Various post-PHF methods from other fields of many-body physics have in recent years been transferred to electronic-structure theory and are under active development. The promising performance of PHF for Heisenberg spin clusters should make the exploration of advanced post-PHF methods worthwhile. Symmetry-projected multiconfiguration approaches could ameliorate the size-extensivity problem and give access to excited states, thus opening the way towards more accurate and comprehensive studies of Heisenberg spin clusters based on symmetry-projection methods.

ACKNOWLEDGMENTS

S.G.T. thanks M. Kaupp for generous support in the early stages of this project and the German Academic Exchange Service (DAAD) for a scholarship.

[1] A. Bencini and D. Gatteschi, *Electron Paramagnetic Resonance of Exchange Coupled Systems* (Springer-Verlag, Berlin, 1990).
[2] J. Schnack and J. Ummethum, Polyhedron **66**, 28 (2013).
[3] S. R. White, Phys. Rev. Lett. **69**, 2863 (1992).
[4] A. Müller, S. Sarkar, S. Q. N. Shah, H. Bögge, M. Schmidtmann, S. Sarkar, P. Kögerler, B. Hauptfleisch, A. X. Trautwein, and V. Schünemann, Angew. Chemie Int Ed. **38**, 3238 (1999).
[5] A. M. Todea, A. Merca, H. Boegge, J. van Slageren, M. Dressel, L. Engelhardt, M. Luban, T. Glaser, M. Henry, and A. Müller, Angew. Chemie Int. Ed. **46**, 6106 (2007).
[6] B. Botar, P. Kögerler, and C. L. Hill, Chem. Commun. **2005**, 3118 (2005).
[7] M. Exler and J. Schnack, Phys. Rev. B **67**, 094440 (2003).
[8] J. Ummethum, J. Schnack, and A. M. Läuchli, J. Magn. Magn. Mater. **327**, 103 (2013).

[9] T. D. Kühner and S. R. White, Phys. Rev. B **60**, 335 (1999).
[10] E. Jeckelmann, Phys. Rev. B **66**, 045114 (2002).
[11] J. Ummethum, J. Nehrkorn, S. Mukherjee, N. B. Ivanov, S. Stuiber, T. Strässle, P. L. W. Tregenna-Piggott, H. Mutka, G. Christou, O. Waldmann, and J. Schnack, Phys. Rev. B **86**, 104403 (2012).
[12] J. Schnack, J. Schulenburg, and J. Richter, Phys. Rev. B **98**, 094423 (2018).
[13] J. Jaklič and P. Prelovšek, Phys. Rev. B **49**, 5065 (1994).
[14] J. Schnack and O. Wendland, Eur. Phys. J. B **78**, 535 (2010).
[15] A. W. Sandvik and J. Kurkijärvi, Phys. Rev. B **43**, 5950 (1991).
[16] P. Henelius and A. W. Sandvik, Phys. Rev. B **62**, 1102 (2000).
[17] J. Schnack and M. Luban, Phys. Rev. B **63**, 014418 (2000).
[18] J. Schnack, M. Luban, and R. Modler, EPL **56**, 863 (2001).
[19] O. Cépas and T. Ziman, Prog. Theor. Phys. Suppl. **159**, 280 (2005).
[20] O. Waldmann, Phys. Rev. B **75**, 012415 (2007).
[21] A. Müller, M. Luban, C. Schröder, R. Modler, P. Kögerler, M. Axenovich, J. Schnack, P. Canfield, S. Bud'ko, and N. Harrison, ChemPhysChem **2**, 517 (2001).
[22] E. Neuscamman and G. K.-L. Chan, Phys. Rev. B **86**, 064402 (2012).
[23] D. J. Klein, Advances in Many-Body Valence-Bond Theory, in *Theoretical and Computational Chemistry* (Elsevier, Amsterdam, 1999) Vol. 6, pp. 403–421.
[24] J. Sanchez-Marin, J. P. Malrieu, and D. Maynau, Int. J. Quantum Chem. **31**, 903 (1987).
[25] N. Guihery, N. Ben Amor, D. Maynau, and J. P. Malrieu, J. Chem. Phys. **104**, 3701 (1996).
[26] D. N. Sheng, Z. Y. Weng, C. S. Ting, and J. M. Dong, Phys. Rev. B **49**, 4279 (1994).
[27] V. Y. Krivnov, I. L. Shamovsky, E. E. Tornau, and A. Rosengren, Phys. Rev. B **50**, 12144 (1994).
[28] N. Flocke, T. G. Schmalz, and D. J. Klein, J. Chem. Phys. **109**, 873 (1998).
[29] S. Li, J. Chem. Phys. **120**, 5017 (2004).
[30] X.-G. Wen, F. Wilczek, and A. Zee, Phys. Rev. B **39**, 11413 (1989).
[31] F. Mila, Frustrated Spin Systems, in *Modeling and Simulation Vol. 5*; edited by E. Pavarini, E. Koch, and P. Coleman (Forschungszentrum Jülich, Berlin, 2015).
[32] C. A. Jiménez-Hoyos, T. M. Henderson, T. Tsuchimochi, and G. E. Scuseria, J. Chem. Phys. **136**, 164109 (2012).
[33] See Supplemental Material at http://link.aps.org/supplemental/10.1103/PhysRevB.105.035147 for additional details on PHF algorithms, the relation between point-group symmetry labels in spin and fermionic representations, and a discussion of exact results for the $s = 1/2, N = 12$ spin ring, which includes O. J. Heilmann and E. H. Lieb, Ann. N. Y. Acad. Sci. **172**, 584 (1971); J. Yoon and E. I. Solomon, Inorg. Chem. **44**, 8076 (2005).
[34] P.-O. Löwdin, Phys. Rev. **97**, 1509 (1955).
[35] I. Mayer, Adv. Quantum Chem. **12**, 189 (1980).
[36] J.-P. Blaizot and G. Ripka, *Quantum Theory of Finite Systems* (The MIT Press, Cambridge, MA, 1985).
[37] H. Fukutome, Int. J. Quantum Chem. **20**, 955 (1981).
[38] J. L. Stuber and J. Paldus, *Symmetry Breaking in the Independent Particle Model, in Fundamental World of Quantum Chemistry: A Tribute Volume to the Memory of Per-Olov Löwdin*; edited by E. J. Brändas, and E. S. Kryachko (Kluwer Academic Publishers, Dordrecht, The Netherlands, 2003).
[39] P. Rivero, C. A. Jiménez-Hoyos, and G. E. Scuseria, J. Phys. Chem. B **117**, 12750 (2013).
[40] K. Samanta, C. A. Jiménez-Hoyos, and G. E. Scuseria, J. Chem. Theory Comput. **8**, 4944 (2012).
[41] P. Rivero, C. A. Jiménez-Hoyos, and G. E. Scuseria, J. Phys. Chem. A **117**, 8073 (2013).
[42] T. Stein, C. A. Jiménez-Hoyos, and G. E. Scuseria, J. Phys. Chem. A **118**, 7261 (2014).
[43] S. Ghassemi Tabrizi, A. V. Arbuznikov, C. A. Jimenez-Hoyos, and M. Kaupp, J. Chem. Theory Comput. **16**, 6222 (2020).
[44] G. E. Scuseria, C. A. Jiménez-Hoyos, T. M. Henderson, K. Samanta, and J. K. Ellis, J. Chem. Phys. **135**, 124108 (2011).
[45] J. Hendeković, Int. J. Quant. Chem. **8**, 799 (1974).
[46] J. Hendeković, Int. J. Quant. Chem **12**, 781 (1977).
[47] M. M. Tinkham, *Group Theory and Quantum Mechanics* (McGraw-Hill, New York, 1964).
[48] J. K. Percus and A. Rotenberg, J. Math. Phys. **3**, 928 (1962).
[49] K. W. Schmid, T. Dahm, J. Margueron, and H. Müther, Phys. Rev. B **72**, 085116 (2005).
[50] P. J. Lestrange, D. B. Williams-Young, A. Petrone, C. A. Jiménez-Hoyos, and X. Li, J. Chem. Theory Comput. **14**, 588 (2018).
[51] C. A. Jiménez-Hoyos, R. Rodríguez-Guzmán, and G. E. Scuseria, J. Phys. Chem. A **118**, 9925 (2014).
[52] K. W. Schmid, Prog. Part. Nucl. Phys. **52**, 565 (2004).
[53] R. Rodríguez-Guzmán, K. W. Schmid, C. A. Jiménez-Hoyos, and G. E. Scuseria, Phys. Rev. B **85**, 245130 (2012).
[54] R. Rodríguez-Guzmán, C. A. Jiménez-Hoyos, R. Schutski, and G. E. Scuseria, Phys. Rev. B **87**, 235129 (2013).
[55] R. Rodríguez-Guzmán, C. A. Jiménez-Hoyos, and G. E. Scuseria, Phys. Rev. B **90**, 195110 (2014).
[56] R. Rodríguez-Guzmán, C. A. Jiménez-Hoyos, and G. E. Scuseria, Phys. Rev. B **89**, 195109 (2014).
[57] T. Tsuchimochi and S. L. Ten-no, J. Chem. Theory Comput. **15**, 6688 (2019).
[58] Z.-X. Liu, Y. Zhou, and T.-K. Ng, Phys. Rev. B **81**, 224417 (2010).
[59] Z.-X. Liu, Y. Zhou, and T.-K. Ng, Phys. Rev. B **82**, 144422 (2010).
[60] M. Serbyn, T. Senthil, and P. A. Lee, Phys. Rev. B **84**, 180403(R) (2011).
[61] M. L. Baez and J. Reuther, Phys. Rev. B **96**, 045144 (2017).
[62] A. Singh, Phys. Rev. B **43**, 3617 (1991).
[63] O. Waldmann, Phys. Rev. B **61**, 6138 (2000).
[64] R. A. Klemm and D. V. Efremov, Phys. Rev. B **77**, 184410 (2008).
[65] S. Ghassemi Tabrizi, A. V. Arbuznikov, and M. Kaupp, Chem. Eur. J. **24**, 4689 (2018).
[66] C. Raghu, I. Rudra, D. Sen, and S. Ramasesha, Phys. Rev. B **64**, 064419 (2001).
[67] N. P. Konstantinidis, Phys. Rev. B **72**, 064453 (2005).
[68] R. Schnalle and J. Schnack, Int. Rev. Phys. Chem. **29**, 403 (2010).
[69] T. Heitmann and J. Schnack, Phys. Rev. B **99**, 134405 (2019).
[70] P. Pulay, J. Comput. Chem. **3**, 556 (1982).
[71] C. A. Jiménez-Hoyos, Ph.D. thesis, Rice University, Houston, TX, 2013.

[72] V. I. Lebedev and D. N. Laikov, Dokl. Math. **59**, 477 (1999).
[73] J. C. Bonner and M. E. Fisher, Phys. Rev. **135**, A640 (1964).
[74] J. B. Parkinson and J. C. Bonner, Phys. Rev. B **32**, 4703 (1985).
[75] A. Moreo, Phys. Rev. B **35**, 8562 (1987).
[76] H. Q. Lin, Phys. Rev. B **42**, 6561 (1990).
[77] J. Schnack, Contemp. Phys. **60**, 127 (2019).
[78] H.-J. Schmidt and M. Luban, J. Phys. A **36**, 6351 (2003).
[79] O. Waldmann, Phys. Rev. B **65**, 024424 (2001).
[80] B. Bernu, P. Lecheminant, C. Lhuillier, and L. Pierre, Phys. Rev. B **50**, 10048 (1994).
[81] M. Axenovich and M. Luban, Phys. Rev. B **63**, 100407(R) (2001).
[82] C. A. Jiménez-Hoyos, R. R. Rodríguez-Guzmán, T. M. Henderson, and G. E. Scuseria, arXiv:2004.05047.
[83] T. M. Henderson, C. A. Jimènez-Hoyos, and G. E. Scuseria, J. Chem. Theory Comput. **14**, 649 (2018).
[84] J. Hendeković and K. Vasudevan, Theor. Chim. Acta **39**, 119 (1975).
[85] C. A. Jiménez-Hoyos, R. Rodríguez-Guzmán, and G. E. Scuseria, Phys. Rev. A **86**, 052102 (2012).
[86] J. Ummethum, Ph.D. thesis, Bielefeld University, Germany, 2012.
[87] D. Coffey and S. A. Trugman, Phys. Rev. Lett. **69**, 176 (1992).
[88] N. P. Konstantinidis, Phys. Rev. B **80**, 134427 (2009).
[89] J. Schnack, Dalt. Trans. **39**, 4677 (2010).
[90] C. Schröder, H.-J. Schmidt, J. Schnack, and M. Luban, Phys. Rev. Lett. **94**, 207203 (2005).
[91] N. P. Konstantinidis, Phys. Rev. B **76**, 104434 (2007).
[92] N. P. Konstantinidis, J. Phys. Condens. Matter **27**, 76001 (2015).
[93] J. Schnack, H.-J. Schmidt, J. Richter, and J. Schulenburg, Eur. Phys. J. B **24**, 475 (2001).
[94] J. Schulenburg, A. Honecker, J. Schnack, J. Richter, and H.-J. Schmidt, Phys. Rev. Lett. **88**, 167207 (2002).
[95] D. Coffey and S. A. Trugman, Phys. Rev. B **46**, 12717 (1992).
[96] M. Ozaki and H. Fukutome, Prog. Theor. Phys. **60**, 1322 (1978).